Microstructure and hydrogen dynamics in hydrogenated amorphous silicon carbides

J. Shinar
Ames Laboratory–USDOE and Department of Physics and Astronomy, Iowa State University, Ames, Iowa 50011

R. Shinar
Microelectronics Research Center, Iowa State University, Ames, Iowa 50011

D. L. Williamson
Department of Physics, Colorado School of Mines, Golden, Colorado 80401

S. Mitra
Department of Engineering Physics, University of Tulsa, Tulsa, Oklahoma 74104

H. Kavak
Microelectronics Research Center, Iowa State University, Ames, Iowa 50011
and Physics Department, Cukurova University, 101330 Adana, Turkey

V. L. Dalal
Microelectronics Research Center, Iowa State University, Ames, Iowa 50011
and Department of Electrical and Computer Engineering, Iowa State University, Ames, Iowa 50011
(Received 16 March 1999)

Small angle x-ray scattering (SAXS) and deuterium secondary-ion-mass spectrometry (DSIMS) studies of the microstructure and hydrogen dynamics in undoped rf-sputter-deposited (RFS) and undoped and boron-doped electron-cyclotron-resonance-deposited (ECR) hydrogenated amorphous silicon carbides (a-$Si_{1-x}C_x$:H) are described. In the RFS carbides with $x \leqslant 19$ at. %, the SAXS indicated that the films contained elongated features larger than 20 nm with preferred orientation, consistent with a residual columnarlike growth of the films. In addition, the SAXS also included a clear nanostructural component consistent with roughly spherical nanovoids ~ 1.1 nm in diameter, of total content $0.5 \leqslant C_{nV} \leqslant 1.0$ vol. %. C_{nV} increased by $\sim 100\%$ after isochronal 1-h annealing at 300, 350, and 375 °C, followed by further annealing for 2–15 hours at 375 °C. The growth of C_{nV} was apparently due largely to a $\sim 20\%$ increase in the average void diameter. This growth was noticeably weaker than in similarly fabricated a-Si:H. In RFS carbides with $x \leqslant 3$ at. %, the DSIMS yielded power-law time dependent H diffusion constants $D(t) = D_{00}(\omega t)^{-\alpha}$, where the dispersion parameter α varied from 0 to $\sim 0.5 \pm 0.1$ among the samples, but was temperature independent at $350\,°\text{C} \leqslant T \leqslant 475\,°\text{C}$. The moderate values of α are consistent with the moderate initial nanovoid contents $C_{nV} \leqslant 1.0$ vol. % determined by SAXS. The weak dependence of α on T is consistent with the weaker growth of the SAXS with annealing as compared to a-Si:H. The values of activation energy $E_a(1000\ \text{Å})$ for a diffusion length $L = 1000$ Å among the different films were ~ 1.7, ~ 1.4, and ~ 0.65 eV. While the first two values are similar to those found in a-Si:H, the nature of the anomalously low value of ~ 0.65 eV is not clear. In undoped ECR a-$Si_{0.86}C_{0.14}$:H, $D(t)$ exhibited a similar power-law time dependence, but α decreased from ~ 0.3 at 350°C and 400 °C to ~ 0.1 at 450°C, also consistent with a low C_{nV}. Thus, in spite of the high-C content, the behavior of α was similar to that of typical a-Si:H at lower temperatures, where it decreases at $T \leqslant 350\,°\text{C}$. However, $E_a(1000\ \text{Å})$ was an anomalously low ~ 1.0 eV. The evolution of the infrared (IR) spectra of both the RFS and ECR films showed that during annealing the Si-bonded H content decreases relative to the C-bonded H content, consistent with a transfer of H from Si- to C-bonded sites or hydrogen evolution. In addition, the reduction in the 2000-cm^{-1} band characteristic of bulk-like Si-H group was much greater than the reduction of the 2100-cm^{-1} band characteristic of surface Si-H, O-Si-H, and C-Si-H groups. Boron doping of the ECR carbides also reduced the bulklike Si-bonded H content, suggesting that it induces nanovoids, consistent with the observed suppression of long-range motion of most of the H and D atoms. However, a small fraction of the H atoms appeared to undergo fast diffusion, reminiscent of the fast diffusion in B-doped a-Si:H. [S0163-1829(99)07247-1]

I. INTRODUCTION

A considerable number of small angle x-ray scattering (SAXS) studies of the microstructure[1–11] and secondary ion mass spectrometry (SIMS) studies of hydrogen diffusion in hydrogenated amorphous Si (a-Si:H) and related materials have been reported to date.[12–31] The analyses of the SAXS provided a quantitative measure of the distribution of nanovoid and microvoid shapes and sizes, their preferred orientation, if any, and the overall void content.[9–11] One study com-

bined SAXS and infrared (IR) measurements of the Si-H bond content and configuration to determine the correlation between the dynamics of the Si network microstructure and that of the hydrogen.[10] It demonstrated a strong correlation between the decreasing Si-bonded H content C_{Si-H} and the growth of the nanovoid content C_{nV} during annealing at temperatures $T \leqslant 430\,^{\circ}\mathrm{C}$.

The deuterium SIMS (DSIMS) results showed that the H diffusion constant is generally time-dependent,[14–20,22,28] usually decreasing with time t as

$$D(t) = D_{00}(\omega t)^{-\alpha}, \tag{1}$$

where the dispersion parameter $0 \leqslant \alpha < 1$. $D(t)$ is determined experimentally by fitting the DSIMS profiles to a complementary error function[17,18,22,28,32]

$$c(x,t) = n_0 \mathrm{erf}\, c\left[\frac{x}{2\sqrt{\langle r^2(t)\rangle}}\right], \tag{2}$$

where

$$\langle r^2(t)\rangle \equiv \int_0^t D(\tau)\,d\tau = \frac{D_{00}(\omega t)^{1-\alpha}}{\omega(1-\alpha)} \equiv r_0^2 t^{1-\alpha} \tag{3}$$

is the mean-square displacement of the diffusing atoms during the (annealing) time t. From Eqs. (2) and (3) it is clear that as $\alpha \to 1$, $\langle r^2(t)\rangle$ becomes time independent and $D(t) \to 0$. The time dependence of $D(t)$ was previously attributed to the multiple-trapping mechanism.[15,16] In the case of an exponential distribution of H trap energies $n_t(E) = n_0 \exp(-E/E_0)$, with width $E_0 = kT_0$, α should decrease with increasing temperature T as

$$\alpha = 1 - T/T_0 \tag{4}$$

In p-type boron-doped glow-discharge deposited (GD) a-Si:H, the characteristic temperature T_0 was experimentally determined to be ~ 600 K.[15] However, subsequent work demonstrated that α increases sharply with increasing nanovoid and microvoid content C_{nV} of the films;[17–19,22] a sufficiently high C_{nV} suppressed the long-range motion of H and D atoms.[17] In addition, some theoretical work showed that the assumption of an exponential distribution of H site energies, usually invoked in the multiple-trapping mechanism, should lead to negative values of α.[33] This sharp contrast with the positive values observed in carrier mobility measurements results from the contrasting initial conditions, where the energies of the H atoms are close to their equilibrium distribution whereas those of the injected carriers are much higher.[33] Within that revised multiple trapping scenario, positive values of α consequently suggested that structural relaxation processes occurring during the diffusion were affecting the distribution of site energies and thus the value of α as well. Other experimental work showed that while at $T \leqslant 350\,^{\circ}\mathrm{C}$ α does generally decrease with increasing T [although not in the form given by Eq. (4)],[22,28] at higher temperatures it increases with increasing T.[20,28] In some a-Si:H films, where C_{Si-H} was 3–5 at. %, α was negative for $300 \leqslant T \leqslant 380\,^{\circ}\mathrm{C}$.[28] The overall picture that emerged from these various studies consequently suggested that α is largely determined not only by C_{nV}, but also by dynamical Si network relaxation processes which probably occur at $T \geqslant 250\,^{\circ}\mathrm{C}$. Indeed, Roorda *et al.*[34] showed that structural relaxation processes in Si amorphized by ion implantation can be detected by differential scanning calorimetry at temperatures as low as 400 K. Finally, the relation between H diffusion and structural relaxation processes, as characterterized by the behavior of C_{nV}, was confirmed by the SAXS study mentioned above.[10] It demonstrated a very strong correlation between C_{nV} and C_{Si-H} during hydrogen evolution at high temperatures. Specifically, it showed that in undoped rf-sputter-deposited (RFS) films of various initial void contents, at $T \geqslant 350\,^{\circ}\mathrm{C}$ C_{nV} sharply increases—consistent with the observed increase in α—as C_{Si-H} sharply decreases.

TABLE I. The CH_4 partial pressure P_{CH_4} during deposition, the carbon content x, and the initial Si-bonded H-content C_{Si-H} of the rf sputter-deposited a-$Si_{1-x}C_x$:(H,D)/a-$Si_{1-x}C_x$:H films (see Sec. II of text). All samples were deposited by rf sputtering a 6″ diameter Si target in 10 mtorr Ar, 0.5 mtorr H_2, 10^{-5} - $1.8.10^{-5}$ torr D_2, and varying CH_4 plasma at an rf power $P = 400$ W, with a target-to-substrate distance of ~ 1.25″.

Sample	P_{CH_4} (torr) (±10%)	x (at. %) (±20%)	C_{Si-H} (at. %) (±1.0)
RFS1	5×10^{-6}	2.2 [b]	
RFS2	1×10^{-6}	2.0 [a], 3 [b]	
RFS3	1.2×10^{-6}	1.6 [a]	12.3
RFS4	6×10^{-6}	3.1±0.7 [a]	14.0
RFS5	1.6×10^{-5}	5.7 [a]	12.5
RFS6	3.4×10^{-5}	2.9 [a]	
RFS7	7.5×10^{-5}	6.0 [a], 6.2 [b]	16.8
RFS8	1.6×10^{-4}	7.1 [a], 7.4 [b b]	9.0
RFS9		19.0 [a]	

[a]From EPMA.
[b]From Auger spectroscopy.

Due to the crucial role of hydrogen dynamics in determining the properties of a-Si:H and the importance of hydrogenated amorphous silicon carbides (a-$Si_{1-x}C_x$:H) in photovoltaic devices and other applications, a combined IR, SAXS, and DSIMS study of H and microstructure dynamics in the carbides is highly desirable. This paper describes such a study in undoped RFS and undoped and boron-doped electron cyclotron resonance-deposited (ECR) a-$Si_{1-x}C_x$:H. The RFS films were fabricated by sputtering a Si target in Ar, H_2, and CH_4 (see Sec. II below and Table I for a summary of the deposition conditions). The ECR films were deposited from SiH_4 and CH_4 precursors. The experimental procedure is described briefly in Sec. II below; additional details may be found elsewhere.[35,36] The SAXS results indicated that the RFS carbides with $x \leqslant 19$ at. % contained elongated features larger than 20 nm with preferred orientation, consistent with a residual columnarlike growth of the films. The SAXS also included a clear nanostructural component consistent with roughly spherical nanovoids ~ 1 nm in diameter, with a total content of 0.5 - 1.0 vol. %, which more than doubled after annealing at temperatures up to 375 °C or 420 °C. This growth of the nanovoid content was,

however, weaker than in similarly fabricated RFS a-Si:H.

The DSIMS results showed that for the undoped RFS films of C content $x \leqslant 3$ at. %, the initial void content $C_{nV0} \leqslant 1.0$ vol. % and the content after annealing $C_{nV} \leqslant 2.0$ vol. % were sufficiently low to enable long-range H motion. The values of α were low to moderate ($\leqslant 0.60$) and essentially temperature independent for $T \geqslant 350\,^{\circ}$C. This near invariance with T is consistent with the SAXS measurements, which indicated that the network dynamics are weaker than those of a-Si:H. The undoped ECR a-$Si_{0.86}C_{0.14}$:H exhibited clear H diffusion at $T \geqslant 350\,^{\circ}$C; the behavior of α was similar to that of typical a-Si:H at lower T. As expected, the IR spectra suggested that as H diffuses, it is transferred from Si- to C-bonded sites. Finally, the observations that boron doping of the ECR carbides reduces the bulk-like Si-bonded H content and suppresses the long-range motion of most of the H atoms is consistent with a larger C_{nV}. However, a small fraction of the H atoms appeared to undergo fast diffusion, reminiscent of B-doped a-Si:H.

II. EXPERIMENTAL PROCEDURE

Bilayer RFS a-$Si_{1-x}C_x$:(H,D)/a-$Si_{1-x}C_x$:H films were fabricated by 13.56 MHz rf sputtering of an undoped polycrystalline 6'' diameter Si target $\sim$1.25'' above the Si wafer, Corning 7059 glass, and Al foil substrates in an Ar, H_2, and CH_4 plasma.[35] The substrates were heated only by the plasma; the substrate temperature T_s was estimated to be $150 \leqslant T_s \leqslant 200\,^{\circ}$C.[35] The deposition conditions are summarized in Table I.

Undoped and boron doped bilayer ECR a-$Si_{1-x}C_x$:(H,D)/a-$Si_{1-x}C_x$:H films were fabricated on either SnO_2-coated glass or a Si wafer using a system described elsewhere.[36,37]

SAXS measurements were conducted on the RFS films codeposited with the other films on 10 μm-thick, high-purity (99,999%) Al foil; they were annealed in a tube furnace under flowing high purity He. The analysis of the SAXS, which yields information on the microstructure of the samples and C_{nV}, is given in Sec. III A 1 below. Additional details can be found elsewhere.[7,9–11]

For IR and DSIMS measurements, the films deposited on Si wafers were annealed in sealed evacuated pyrex tubes. C_{Si-H} was determined from the 640 cm^{-1} IR wagging mode absorption.[17,18,28,35,38] Its initial value in some of the RFS films is given in Table I. Since the determination of the integrated intensity of this band required its deconvolution from the Si-CH_n bands at 770 - 1000 cm^{-1} (see below),[39–41] the estimated error in C_{Si-H} is a relatively large $\pm 15\%$. In the ECR films, C_{Si-H} was estimated to be $\sim$12 at. % in samples ECR1–ECR4, which were deposited at $T_s = 250\,^{\circ}$C, and $\sim$6 at. % in sample ECR5, which was deposited at $T_s = 350\,^{\circ}$C (see Table II). Since the 3000 cm^{-1} C-H stretch band was unobservable, probably due to its weak oscillator strength, the C-bonded H content C_{C-H} could not be determined directly. Although the Si-CH_n and C-H wagging mode bands at $\sim$770 and $\sim$1000 cm^{-1}, respectively,[39–41] do provide a measure of C_{C-H}, it is only qualitative due to the overlap with the strong 640 cm^{-1} Si-H wag mode and the (albeit weak) 850 and 890 cm^{-1} Si-H_2 bending or scissors doublet.[10,17,22,28,35,38]

TABLE II. Boron and initial Si-bonded H content C_B and C_{Si-H} of the electron cyclotron resonance (ECR)-deposited films, grown on SnO_2 or a Si wafer. Samples ECR1–ECR4 were deposited at a substrate temperature $T_s = 250\,^{\circ}$C; sample ECR5 was deposited at $T_s = 350\,^{\circ}$C.

Sample	C_B (at. %) $\pm 30\%$	C_{Si-H} (at. %) $\pm 20\%$
ECR1	0	$\sim$12
ECR2	$\sim$0.01	$\sim$12
ECR3	0.2	$\sim$12
ECR4	0.6	$\sim$12
ECR5	0	$\sim$6

While the integrated intensity of the 640 cm^{-1} band is a reliable measure of C_{Si-H} and the $\sim$770 and $\sim$1000 cm^{-1} bands are related to the C-bonded H content, the 2000–2150 cm^{-1} Si-H stretch band provides insight into the nature of the Si-H bonding configuration. The 2000 cm^{-1} band is the vibration frequency of a Si-H configuration embedded in the a-Si network.[35,38] The 2080–2150 cm^{-1} band is usually associated with the vibration of Si-H bonds on the internal surfaces of nanovoids or microvoids, Si-H bonds in SiH_2 and SiH_3 configurations, or of H bonded to Si which is bonded to O or C.[25,28]

The carbon content x of the RFS films was determined in Ames by Auger spectroscopy using a PHI 545 Auger microprobe, or at the National Renewable Energy Laboratory by electron probe microanalysis (EPMA). Auger measurements yielded a carbon content $x \approx 14$ at. % in all of the ECR samples, consistent with the measured energy gap of $\sim$2 eV. The ECR films also contained 0.1–0.3 at. % oxygen, independent of doping or annealing. The boron doping levels were determined by SIMS. The composition of the RFS and ECR films is summarized in Tables I and II, respectively.

TABLE III. The EPMA-determined carbon content x and the initial values of the flotation density ρ (g/cm^3), Porod Constant A (eu/nm^3) (see Eq. (5)), the q-independent diffuse scattering intensity I_D (eu), the total integrated SAXS Q_{SAXS} (10^{24} eu/cm^3), the contribution of the nanovoids to the integrated SAXS Q_N (10^{24} eu/cm^3), and the resulting void content C_{nV0} (vol. %) [see Eq. (6)] of the RFS a-$Si_{1-x}C_x$:H samples.

Sample	x $\pm 15\%$	ρ ± 0.005	A $\pm 5\%$	I_D $\pm 5\%$	Q_{SAXS} $\pm 5\%$	Q_N $\pm 5\%$	C_{nV0} $\pm 5\%$
RFS2	2.0	2.127	13	13	2.2	1.8	1.0
RFS3	1.6	2.156	8	12	1.2	0.9	0.5
RFS4	3.1	2.117	12	20	2.0	1.6	0.9
RFS5	5.7	2.132	23	20	1.8	1.2	0.7
RFS6	2.9	2.146	18	22	1.8	1.4	0.8
RFS7	6.0	2.136	12	18	1.95	1.5	0.9
RFS8	7.1	2.233	15	17	1.25	0.9	0.5
RFS9	19.0	2.176	15	25	2.2	1.5	0.8

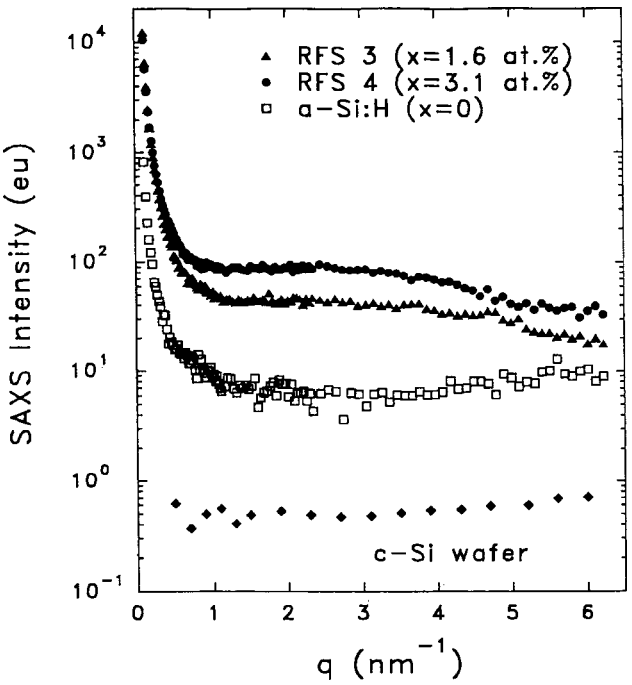

FIG. 1. The SAXS intensity (in absolute electron units eu) of samples RFS3 and RFS4, as compared to a typical glow-discharge-deposited a-Si:H with $C_{Si-H} \sim 8$ at. % and a single crystal Si wafer. Note the steep rise of $I(q)$ with decreasing q at low q. The SAXS analysis yields that $C_{nV}=0.5$ and 0.9 vol. % in the two films, respectively.

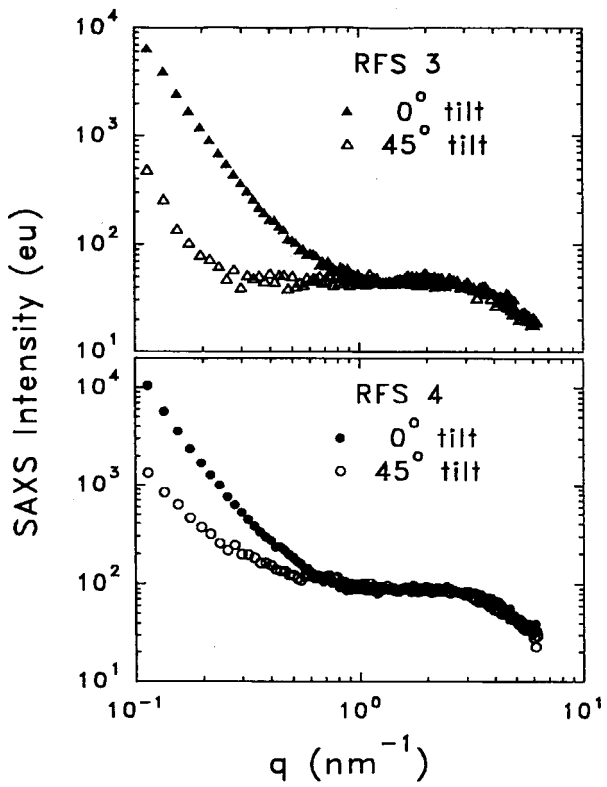

FIG. 2. The effects of the tilt angle on the SAXS of RFS3 and RFS4. The log-log scale reveals that the effect is weak at high q but pronounced at low q, consistent with relatively large elongated features with a preferred orientation, i.e., reminiscent of columns, which are $\geqslant 20$ nm in diameter (see text).

III. EXPERIMENTAL RESULTS AND ANALYSIS

A. SAXS and the microstructural dynamics of the RFS films

1. The microstructure of the as-deposited RFS films

Table III lists the EPMA-determined values of the carbon content x of the RFS samples and their densities ρ as measured by flotation. We note that the density of Si is 2.33 g/cm^3 and that of SiC is 3.22 g/cm^3, so the measured densities range from 91% of Si in sample RFS4 to 96% of Si in RFS8. Hence it appears that the role of the morphology and the hydrogen in lowering ρ is much more significant than the role of the carbon in raising it.

Figure 1 shows the SAXS intensity $I(q)$, where $q=(4\pi/\lambda)\sin\theta$ is the x-ray scattering wave vector ($\lambda=0.154$ nm is the x-ray wavelength and 2θ is the scattering angle), of as-deposited samples RFS3 and RFS4, as well as that of a typical GD a-Si:H film with $C_{Si-H} \sim 8$ at. % and a single crystal Si (c-Si) wafer. As clearly seen at low q, $I(q)$ increases steeply with decreasing q. We note that all of the RFS films exhibited this behavior, which can be fit to a contribution $I_L(q)$ of the form appropriate for the line collimation slit geometry used here

$$I_L(q)=A/q^3 \tag{5}$$

known as the ''Porod law.''[9,42] It can be shown to be a general behavior of the ''tail'' (i.e., high q) region of the scattering curve resulting from structural features, which are large relative to the instrumental resolution.[9,42,43] In the present work this resolution corresponds to ~ 20 nm. The ''Porod constant'' A provides a measure of the total surface area of these larger-scale scattering objects. Its values in the as-deposited RFS films are also given in Table III.

Additional information on the existence or absence of any preferred orientation of the structural features may be obtained from tilting SAXS measurements, in which $I(q)$ is measured at different angles of the film with respect to the incident x-ray beam.[9,10,42] Figure 2 shows the effects of the tilt angle on the SAXS of RFS3 and RFS4, which was also observed in samples RFS2, RFS7, RFS8, and RFS9. Although the tilt-angle dependence is weak at high q, it is large for $0.1 \leqslant q \leqslant 1$ nm^{-1}, which corresponds to the large features. Specifically, it shows that A drops sharply upon tilting to 45°, indicating that the large-scale features are highly elongated and have a preferred orientation. We suggest that these features are due to residual columnarlike growth and represent the ''columns,'' which are well known from earlier microstructural studies to be $\geqslant 20$ nm in diameter[9,10] and are defined by lower density regions at the column boundaries. In comparison, the tilting SAXS dependence of films which are truly columnar is significantly stronger.[10] The residual columnarlike morphology should be kept in mind, however, when considering the possible atomic H diffusion paths.

In addition to the Porod term [Eq. (5)], all of the RFS samples showed a clear q-independent diffuse scattering term I_D (see Fig. 1) and a nanostructural contribution $I_N(q)$ to the SAXS.[9,42] The values of I_D are listed in Table III. Figure 1 shows that they are roughly a factor of 2 to 3 higher than those of device-quality GD a-Si:H and roughly two orders of magnitude higher than those of a c-Si wafer. $I_N(q)$

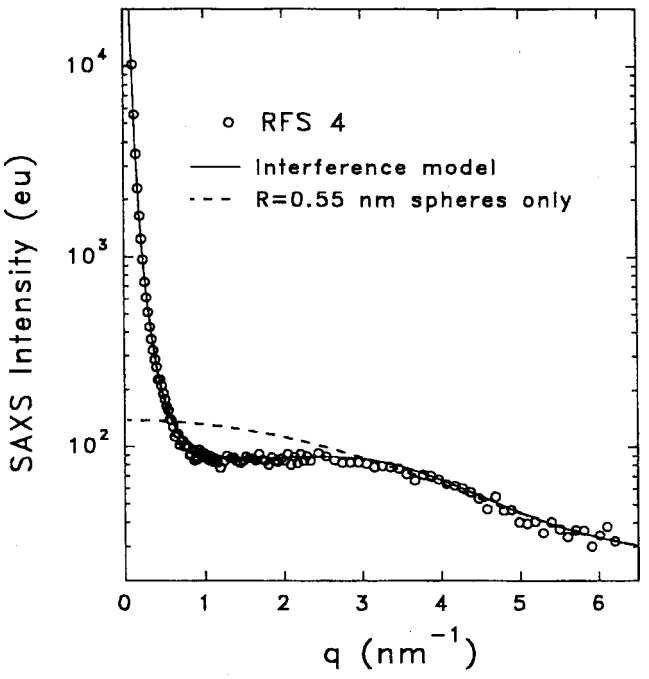

FIG. 3. The fit of the SAXS of as-deposited RFS4 (circles) to Eq. (7) (solid line) in which $I_N(q)$ includes a hard-sphere structure factor based on the Percus-Yevick model. The dashed line shows only the spherical form factor with $R=0.55$ nm.

corresponds to the broad ''shoulder'' in the high-q region of the SAXS. It can be modeled as a spherical particle form factor[42] with radius R and by the Percus-Yevick hard-sphere interaction theory of the structure factor.[9,11] The adjustable parameters of this model are the effective hard-sphere diameter D and the apparent volume fraction v of the particles (nanovoids). This structure factor is needed when SAXS data show a well-defined shoulder or maximum since normally $I(q)$ decreases monotonically with increasing q. The presence of the shoulder or maximum implies that the positions of the scattering objects (nanovoids) are correlated such that scattering interference occurs between them. D and v can be apparently larger than the actual $2R$ and C_{nV} of the nanovoids due to some type of interaction, e.g., solute depletion.[11,43] As previously suggested for a-SiC:H alloys,[9] another type of interaction that could play a role is the local strain fields associated with the nanovoids, inducing correlations in their positions (see Sec. IV A 1 below). If the ''particles'' are indeed nanovoids or nanobubbles containing H_2,[11] then the contribution of $I_N(q)$ to the integrated SAXS Q_N is related to C_{nV} by

$$Q_N \equiv \int_0^\infty I_N(q) q dq = K(\Delta\rho)^2 C_{nV}(1-C_{nV}), \qquad (6)$$

where K is a constant described elsewhere[9,11] and $\Delta\rho$ is the difference between the electron density in the a-$Si_{1-x}C_x$:H network and the nanovoid or nanobubble. Equation (6) is appropriate to the line-slit SAXS geometry. Figure 3 shows the agreement between the total observed SAXS intensity $I(q)$ of as-deposited RFS4 and the sum of the three terms:

$$I(q) = I_L(q) + I_D + I_N(q), \qquad (7)$$

TABLE IV. Q_{SAXS} (10^{24} eu/cm^3, $\pm 5\%$) of samples RFS2 - RFS8 following each annealing step for time t (hours) at temperature T (°C).

$t@T$	RFS2	RFS3	RFS4	RFS5	RFS6	RFS7	RFS8
1@300	2.3	1.3	2.1	1.9	1.9	2.1	1.3
1@350	2.7	1.7	2.6	2.3	2.3	2.6	
1@375	2.9	2.0	2.9	2.6	2.7	2.8	
2@375	3.1	2.2	3.0	2.9	3.2	2.85	
3@375		2.2	3.1			2.8	
5@375		2.4	3.15			3.0	
8@375		2.4	3.35			3.2	
15@375		2.6	3.6			3.4	
1@420	3.8						2.0
2@420	3.9						2.1
4@420	4.1						2.4

where the $I_N(q)$ term includes the Percus-Yevick interference modeling. The excellent agreement clearly justifies this approach in analyzing the observed SAXS. Figure 3 also shows (dashed line) the separate contribution from only the spherical form factor with $R=0.55$ nm, i.e., neglecting the interference effect and the Porod term. The Percus-Yevick model yields $D=1.7$ nm, and $v=15$ vol. % for the fit shown, clearly indicating a hard-sphere interaction distance greater than $2R$.

Table III lists the values of the total integrated intensity of the SAXS, Q_N and C_{nV} of the as-deposited RFS films obtained from Eq. (6). The total integrated SAXS, Q_{SAXS}, is also calculated using $I_L(q)$ with $I_N(q)$ in Eq. (6). However, the integration limits used to calculate Q_N and Q_{SAXS} are the experimental lower and upper limits of q, rather than 0 and ∞ as indicated in Eq. (6). This has a negligible effect on Q_N but obviously limits the contribution of I_L to Q_{SAXS}.

As clearly seen, the values of C_{nV} range from 0.5 to 1.0 vol. %. These values are much higher than those of device-quality GD a-Si:H, which are generally lower than 0.1 vol. % and often $\leqslant 0.01$ vol. %.[9]

2. Annealing effects and microstructural dynamics of the RFS films

The values of Q_{SAXS} of samples RFS2–RFS7 following a sequence of annealing steps are summarized in Table IV and shown vs the temperature and annealing time in Fig. 4. The annealing sequence was chosen to enable a comparison with the behavior of RFS a-Si:H films which were subjected to a similar sequence and monitored by IR and SAXS measurements.[9] As clearly seen, Q_{SAXS} increases monotonically with annealing temperature or time. Note that in all cases Q_{SAXS} increases by $\leqslant 100\%$ from the initial to the most annealed state. In comparison, Q_{SAXS} of RFS a-Si:H increased by more than 200% following similar annealing sequences.[10] Hence, it appears that the inclusion of carbon slows the evolution of the microstructure significantly. However, the dynamics of the microstructure appear to be largely independent of x for $1.6 \leqslant x \leqslant 19$ at. %. This point is discussed in greater detail in Sec. IV A 2

The results of the analyses of the SAXS of the samples following the final annealing step are summarized in Table

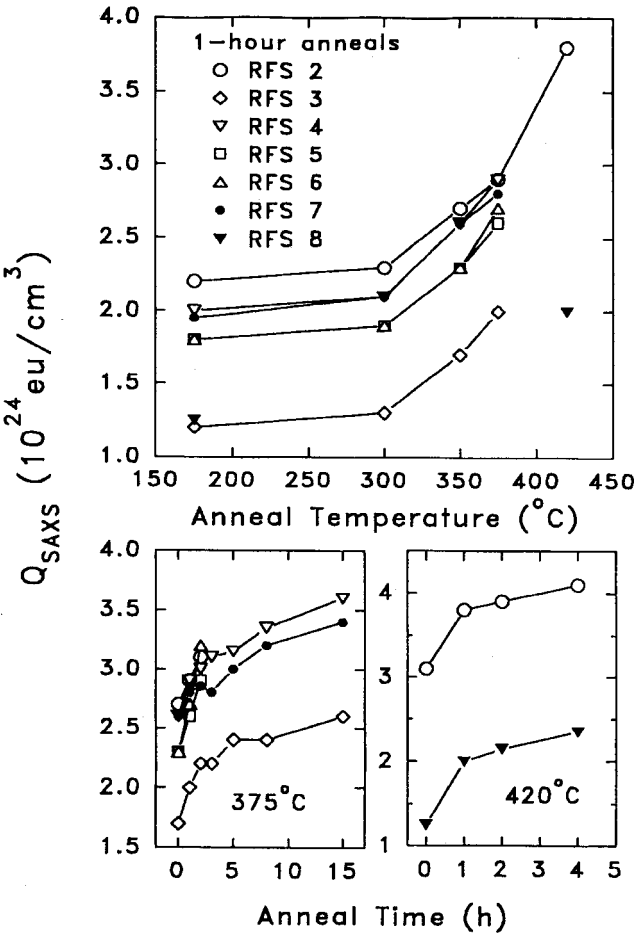

FIG. 4. Total integrated intensity Q_{SAXS} of the RFS films vs annealing temperature and time.

V. Note that the Porod constant A does not change significantly upon annealing (see also Fig. 5). However, I_D decreases by 25%–40% and Q_N, and consequently C_{nV}, increase by 60%–100% after annealing for 2 h at 375 °C and by 100%–200% after annealing for 15 hours at the same temperature. The reduction in I_D is very likely related to the loss of bonded H, which can cause reduced diffuse scattering as demonstrated recently.[11] Figure 5 compares $I(q)$ of RFS4 following annealing for 15 hours at 375°C to that of the as-deposited film. The analysis of $I(q)$ indicated that the initial $R=0.55$ nm average sphere radius of the voids increased to $R=0.65$ nm following annealing (see Fig. 5). Such an increase in the average radius would account for a 65% increase in C_{nV}. Hence, it appears that the expansion of the average void size is the primary process affecting C_{nV} rather than the generation of additional voids. This behavior is similar to that of RFS a-Si:H, where it appeared that the average void size increased significantly.[10] However, in RFS a-Si:H it was also observed that ρ remained essentially unchanged during annealing, leading to the conclusion that the density of the Si network increased accordingly.[10]

TABLE V. The results of the analyses of the SAXS of the RFS samples following the final annealing step listed in Table IV, including the Porod Constant A (eu/nm^3) [see Eq. (6)], the q-independent diffuse scattering intensity I_D (eu), the total integrated SAXS Q_{SAXS} (10^{24} eu/cm^3), the contribution of the nanovoids to the integrated SAXS Q_N (10^{24} eu/cm^3), and the resulting void content C_{nV} (vol. %) [see Eq. (6)].

Sample	x ±15%	ρ ±0.005	A ±5%	I_D ±5%	Q_{SAXS} ±5%	Q_N ±5%	C_{nV} ±5%
RFS2	2.0	2.127	12	8	3.1	2.7	1.6
RFS3	1.6	2.156	12	9	2.9	2.5	1.4
RFS4	3.1	2.117	11	14	3.6	3.2	1.9
RFS5	5.7	2.132	22	12	2.9	2.4	1.4
RFS6	2.9	2.146	18	12	3.3	2.9	1.7
RFS7	6.0	2.136	14	12	3.4	3.0	1.7

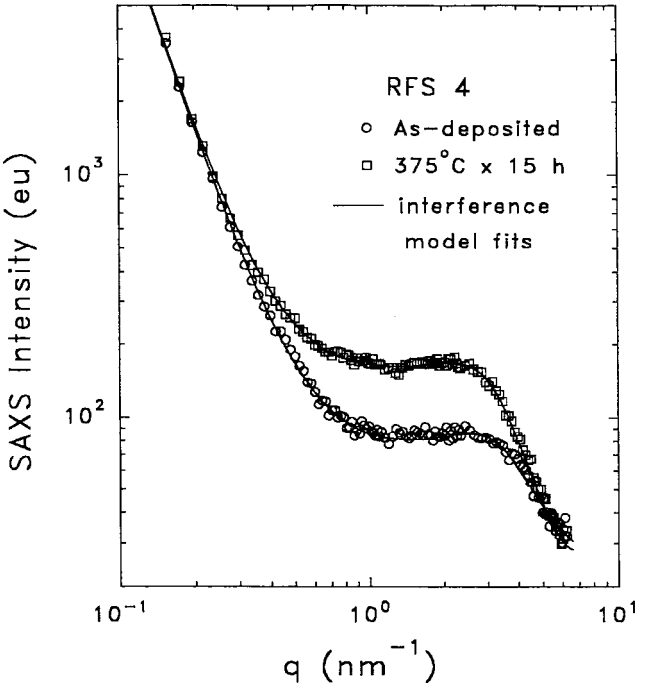

FIG. 5. As-deposited and annealed SAXS of sample RFS4 with interference model fits. These fits yield in the as-deposited film $R=0.55$ nm, $A=12$ eu/nm^3, $I_D=20$ eu, and $C_{nV}=0.9$ vol. % (see Table III); in the annealed film $R=0.65$ nm, $A=11$ eu/nm^3, $I_D=14$ eu, and $C_{nV}=1.9$ vol. % (see Table V).

B. DSIMS measurements of H diffusion in RFS a-Si$_{1-x}$C$_x$:H, $x\leqslant 3$ at. %

Figure 6 shows the DSIMS profile of sample RFS1 following annealing for 12 h at 350 °C; the open circles are the fitted complementary error function. The profiles fo the as-deposited samples were sharp, so ''smearing'' of the profiles following annealing clearly indicates long-range D motion, presumed to be different from H motion only by the conventional isotope effect.

Figures 7–9 show the behavior of $\langle r^2(t)\rangle$ in these films, determined by fitting the profiles to Eq. (2), vs annealing

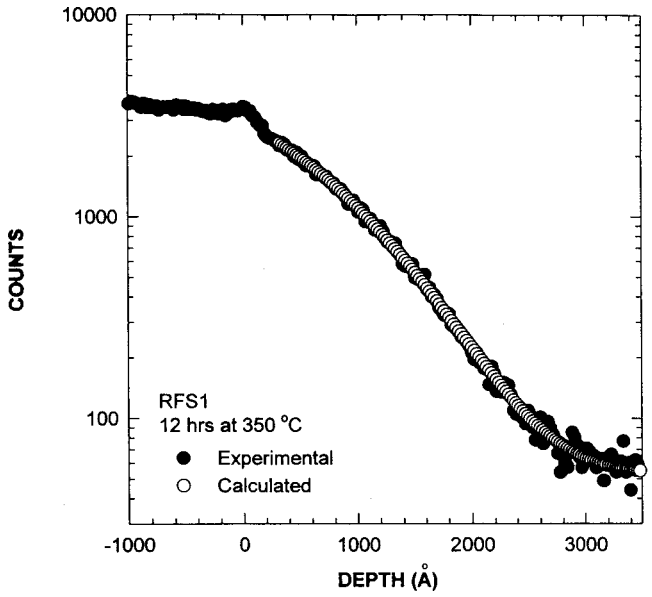

FIG. 6. DSIMS profile of sample RFS1 following annealing for 12 h at 350 °C. The open circles are the fitted complementary error function.

time on a log-log scale at the various annealing temperatures. The values of α [see Eqs. (1)–(3)], determined by a linear best fit of $\log\langle r^2(t)\rangle$ vs $\log t$, are summarized in Table VI. The values of α in RFS2 and RFS3 are quite low and reminiscent of device quality GD a-Si:H.[14,15,19,22] For each sample, the values are all within the error of about ± 0.15 of the average. This suggests that within each sample, the temperature dependence of α is too weak to be determined. This situation is in contrast to that of a-Si:H of low-to-moderate C_{nV}, where α typically decreases with increasing T at $T \leqslant 350$ °C but increases strongly at higher T, regardless of the deposition procedure.[15,20,22,28] The nature of this change in the behavior of α caused by 1.6–3 at. % substitutional C doping is discussed in Sec. IV below.

Starting from Eq. (3) it can be shown that the diffusion constant $D(t_L)$ for the diffusion length

$$L = 2\sqrt{\langle r^2(t)\rangle} \tag{8}$$

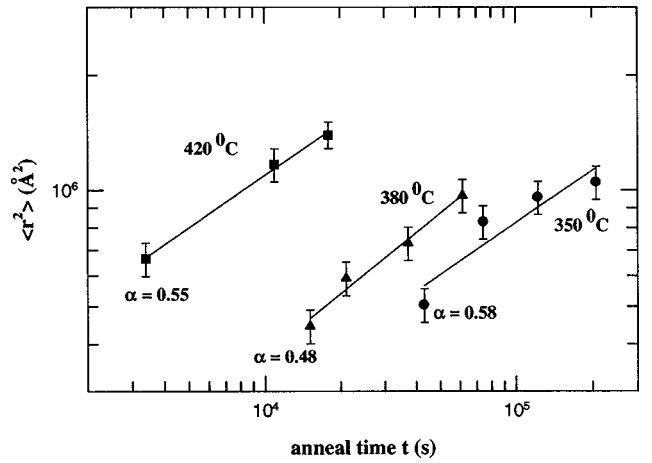

FIG. 7. The values of $\langle r^2(t)\rangle$ in sample RFS1, determined by fitting the profiles to Eq. (2), vs annealing time at the various annealing temperatures. Note the log-log scale.

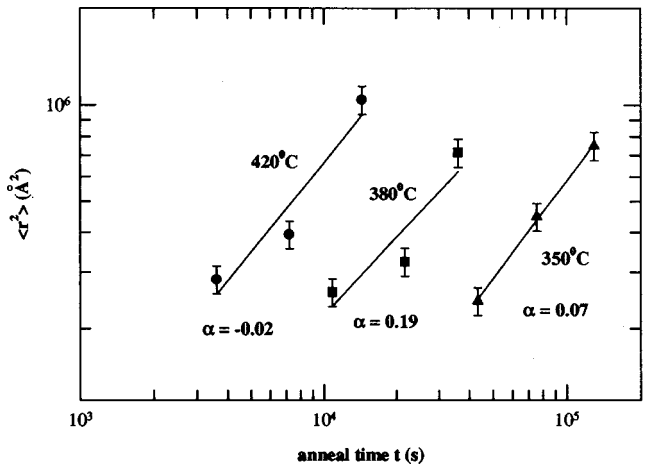

FIG. 8. The values of $\langle r^2(t)\rangle$ in sample RFS2, determined by fitting the profiles to Eq. (2), vs annealing time at the various annealing temperatures. Note the log-log scale.

is given by

$$D(t_L) = \frac{(1-\alpha)L^2}{4t_L}. \tag{9}$$

Hence, for $\langle r^2(t)\rangle = 2.5\times 10^{-11}$ cm^2, $L = 1000$ Å, the diffusion constants obtained from Figs. 7–9 and Eq. (9), which are plotted vs $1/T$ in Fig. 10, yield an activation energy $E_a(1000\ \text{Å})$ of ~ 1.7, ~ 1.4, and ~ 0.65 eV in RFS1, RFS2, and RFS3, respectively. The first two values are similar to those found for a-Si:H;[1,3,4,7,11] the nature of the anomalously low value found for RFS3 is not clear.

In concluding the analysis of the SAXS and DSIMS results of the RFS films, we note that they demonstrate clearly that a residual columnar morphology and a void content C_{nV} which increases from $\leqslant 1$ vol. % in the as-deposited films to $\leqslant 2$ vol. % in the annealed films are not sufficient to suppress the long range motion of deuterium or hydrogen.

C. IR measurements of H evolution and bonding configurations in RFS a-$Si_{1-x}C_x$:H

Figure 11(a) shows typical IR spectra of RFS3 ($x = 1.6$ at. %) as-deposited and following sequential annealing for 1

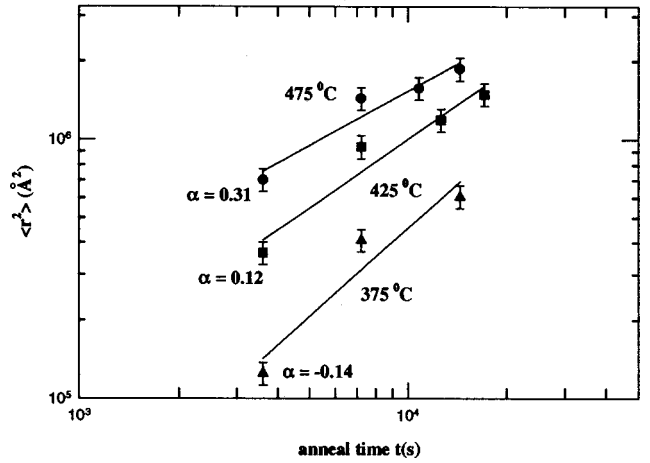

FIG. 9. The values of $\langle r^2(t)\rangle$ in sample RFS3, determined by fitting the profiles to Eq. (2), vs annealing time at the various annealing temperatures. Note the log-log scale.

TABLE VI. Values of the dispersion parameter for diffusion α [see Eq. (1)] in RFS1–RFS3, as determined by fitting the behavior of $\langle r^2(t)\rangle$ obtained from the DSIMS profiles to Eqs. (2) and (3).

Sample RFS1		Sample RFS2		Sample RFS3	
T(°C)	α ($\pm$0.1)	T(°C)	α ($\pm$0.1)	T(°C)	α ($\pm$0.1)
350	0.63	350	0	375	0
380	0.47	380	0.20	425	0.09
420	0.52	420	0.07	475	0.30

h at 300, 350, and 375 °C, followed by additional annealing for a total of 3 hrs and 8 hrs at 375 °C. The Si-H stretch band has a broad ''flat'' peak at 2000–2100 cm^{-1}, due to the overlap of the 2100 and 2000 cm^{-1} bands. There is also a shoulder at $\sim$750 cm^{-1} and peaks at $\sim$910 and $\sim$1000 cm^{-1}, which are usually associated with vibrations of Si-CH_n, Si-O, and (wagging) C-H, respectively, as mentioned in Sec. II above.[39–41]

As Fig. 11(a) shows, during the annealing sequence the 2000 cm^{-1} band weakens relative to the 2100 cm^{-1} band. As discussed in Sec. IV below, this is consistent with detrapping of H atoms from Si-H bonds embedded in the Si network and diffusion to deeper Si-H bond sites at Si-O sites, Si-C sites, or Si sites on internal surfaces of microvoids or nanovoids.

Figure 11(a) also shows that the intensities of the Si-CH_n vibrations at $\sim$770 cm^{-1} and the C-H wagging mode at $\sim$1000 cm^{-1} increase relative to the Si-H wagging mode at 640 cm^{-1}. This behavior is also consistent with the net transfer of hydrogen and deuterium from the shallower Si- to the deeper C-bonded trap sites.

Figure 11(b) shows the evolution of C_{Si-H} in RFS3 (x = 1.6 at. %, with initial nanovoid content C_{nV0} = 0.5 vol. %) as determined by the evolution of the 640 cm^{-1} Si-H wagging mode band.[35,38] C_{Si-H} decreases by 20% from 12.3 $\pm$1.5 at. % to 10$\pm$1.5 at. %, following the annealing steps shown in the figure, consistent with the net transfer of H from Si-bonded sites to the deeper sites mentioned above and evolution of hydrogen from the film.

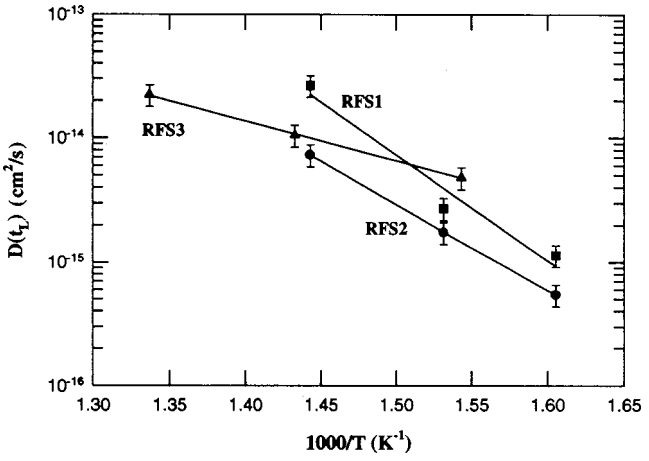

FIG. 10. The diffusion constants $D(t_L)$ for $\langle r^2(t)\rangle$ = 2.5 $\times 10^{-11}$ cm^2, L = 1000 Å, obtained from Figs. 7–9 and Eq. (7), vs 1/T. The slopes yield activation energyies E_a(1000 Å) of $\sim$1.7, $\sim$1.4, and $\sim$0.65 eV for RFS1, RFS2, and RFS3, respectively. The first two values are similar to those found for a-Si:H.[12,14,15,18,22] The latter value, which is anomalously low, is not understood.

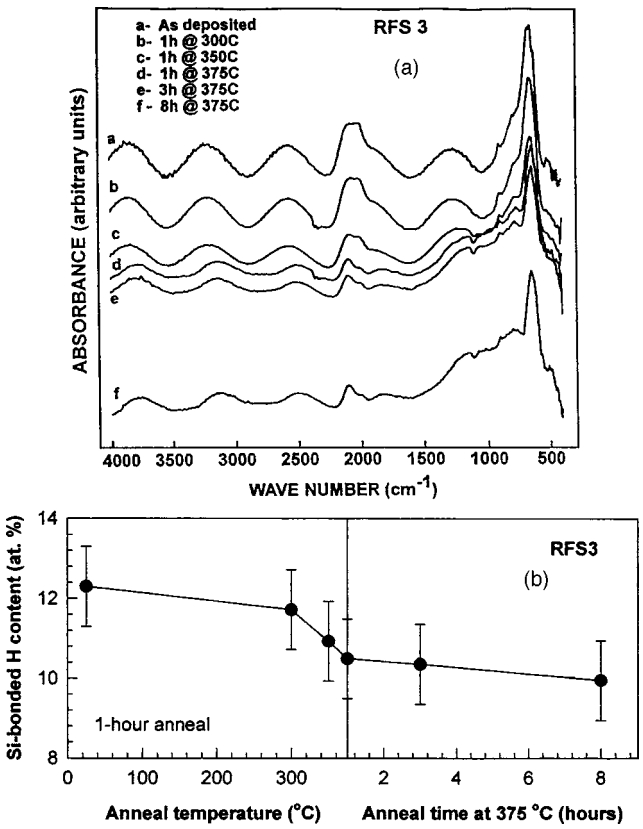

FIG. 11. (a) IR spectra of RFS3, as deposited and annealed sequentially for 1 h at 300, 350, and 375 °C, followed by additional annealing for a total of 3 hrs and 8 hrs at 375 °C. (b) Evolution of C_{Si-H} in RFS3, as determined by the evolution of the 640 cm^{-1} Si-H wagging mode band.

Figures 12–14 show the evolution of the IR spectra and C_{Si-H} in RFS4 (x = 3.0$\pm$0.7 at. %, C_{nV0} = 0.9 vol. %), RFS5 (x = 5.7 at. %, C_{nV0} = 0.7 vol. %), and RFS7 (x = 6.0 at. %, C_{nV0} = 0.9 vol. %), respectively, following the same annealing sequence as RFS3 (see Fig. 11). The Si-H stretch band of as-deposited RFS4 peaks at $\sim$2100 cm^{-1}, but includes a shoulder at $\sim$2000 cm^{-1}. Thus, it appears that in this film the initial fraction of the Si-bonded H atoms embedded in the bulk of the Si network was lower than in RFS3, consistent with the higher carbon content. Interestingly, while the evolution of the 2000–2100 cm^{-1} IR band of RFS4 [Fig. 12(a)], RFS5 [Fig. 13(a)], and RFS7 [Fig. 14(a)] is qualitatively similar to that of RFS3 [Fig. 11(a)], C_{Si-H} decreases by a much larger $\sim$50% in RFS4, from 14$\pm$1 to 6.8$\pm$1 at. %, $\sim$32% in RFS5, from 12$\pm$1 to 8$\pm$1 at. %, and $\sim$34% in RFS7, from 16.8$\pm$1 to 11.0$\pm$1 at. %. While it is difficult to correlate the decrease of C_{Si-H} with x, which is a much higher 5.7 at. % in RFS5 and 6.0 at. % in RFS7 than the 3.0$\pm$0.7 at. % in RFS4, Table VII shows that it does appear to be correlated with C_{nV0} and C_{nV}. This correlation is very plausible since the average distance from a Si-H group to the nearest void surface, where the H may recombine to molecular H_2, decreases with increasing C_{nV0}. This point is discussed in greater detail in Sec. IV below.

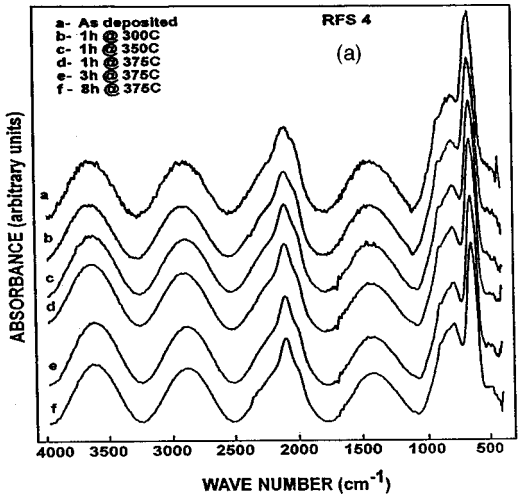

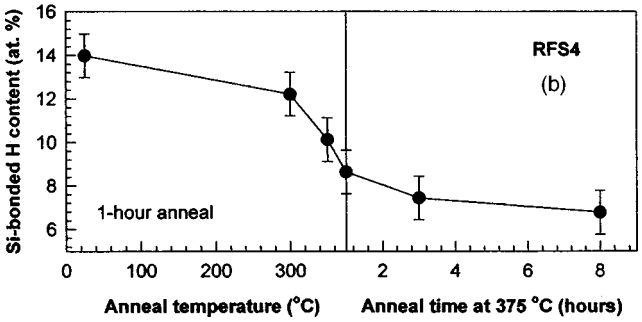

FIG. 12. (a) IR spectra of RFS4, as deposited and annealed sequentially for 1 h at 300, 350, and 375 °C, followed by additional annealing for a total of 3 and 8 h at 375 °C. (b) Evolution of C_{Si-H} in RFS4, as determined by the evolution of the 640 cm^{-1} Si-H wagging mode band.

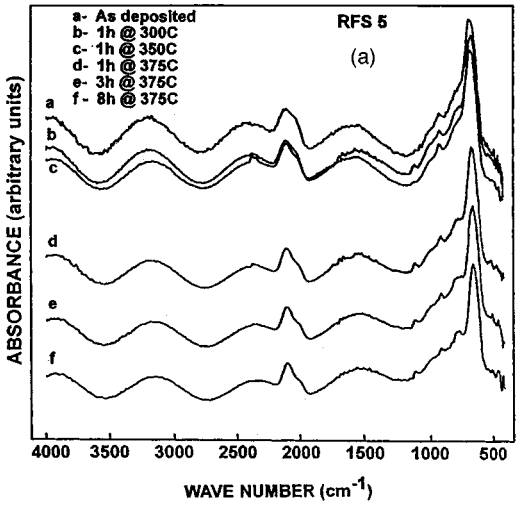

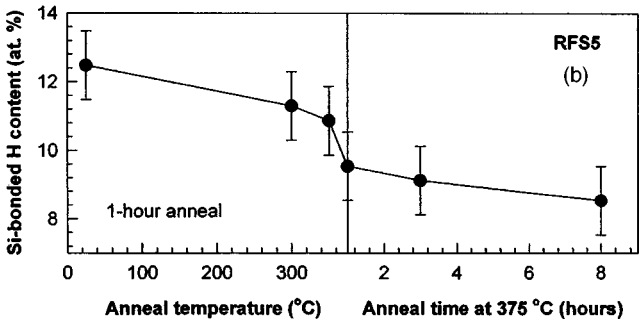

FIG. 13. (a) IR spectra of RFS5, as deposited and annealed sequentially for 1 h at 300, 350, and 375 °C, followed by additional annealing for a total of 3 and 8 h at 375 °C. (b) Evolution of C_{Si-H} in RFS5, as determined by the evolution of the 640 cm^{-1} Si-H wagging mode band.

D. Hydrogen dynamics in undoped ECR a-$Si_{0.86}C_{0.14}$:H

The behavior of the deuterium diffusion distance $\langle r^2(t)\rangle$ vs annealing time t in undoped sample ECR1 at 350, 400, and 450 °C is shown in Fig. 15. A typical DSIMS profile obtained after annealing for 24 h at 400 °C and the complementary error function fit to it are shown in the inset of that figure. As clearly seen, $\langle r^2(t)\rangle$ does indeed behave as a power law function of the diffusion (annealing) time t. The values of α are ~ 0.3, ~ 0.3, and ~ 0.1 at 350, 400, and 450 °C, respectively. As in RFS2 and RFS3 (see Sec. III B above and Table VI) and device-quality a-Si:H,[14,15,19,22] these values are very small and suggest that the void content of ECR1 was relatively low. While α does appear to decrease with increasing temperature, the decrease is very moderate, comparable to the weak increase in α of RFS3 (see Fig. 9 and Table VI).

The behavior of $D(t_L)$ in the undoped ECR films yields an activation energy $E_a(1000\ \text{Å}) \sim 1.0$ eV. As for RFS3, this value is significantly lower than the typical ~ 1.5 eV obtained in a-Si:H at $250 \leqslant T \leqslant 350$ °C.[12,14,22] The nature of this anomalously low value of E_a is not understood and its appearance in both RFS and ECR films deserves further attention.

Figure 16 shows the IR spectrum of sample ECR5 as deposited. Similar to RFS4 (Fig. 12), the Si-H stretch band peaks at ~ 2080 cm^{-1}, i.e., close to the 2100 cm^{-1} band usually associated with Si-H bonds in nanovoids, SiH_2 and SiH_3 configurations, or H bonded to Si which is bonded to O or C (see Sec. II above).[35,38] However, there is a significant shoulder at ~ 2000 cm^{-1}, which is the stretching mode vibration frequency of a Si-H configuration embedded in the a-Si network.[35,38] There is also a shoulder at ~ 750 cm^{-1} and peaks at ~ 910 and ~ 1000 cm^{-1}, consistent with the considerable content of Si-CH_n and C-H configurations, and the presence of oxygen in the films (see Sec. II above).

E. Hydrogen dynamics in boron-doped ECR a-$Si_{0.86}C_{0.14}$:H

Several SIMS depth profiles of sample ECR3 (boron content $C_B \approx 0.2$ at. %), annealed at $T \leqslant 450$ °C and normalized to the maximal D level $C_{D_{max}}$, are shown in Fig. 17. The profiles clearly show that the diffusion of most of the H and D atoms is suppressed, even at $T = 450$ °C. However, the large ''tail'' of the profile in the undeuterated layer indicates rapid diffusion of a small fraction of the D atoms in that region. This point is discussed in relation to the exchange model of Kemp and Branz[30,31] in Sec. IV E.

Figures 16(b)–16(e) show the IR spectra of sample ECR3 annealed at various temperatures. As in the RFS films, the ~ 2000 cm^{-1} component of the Si-H stretch band weakens relative to 2100 cm^{-1} component while, as in RFS3, the

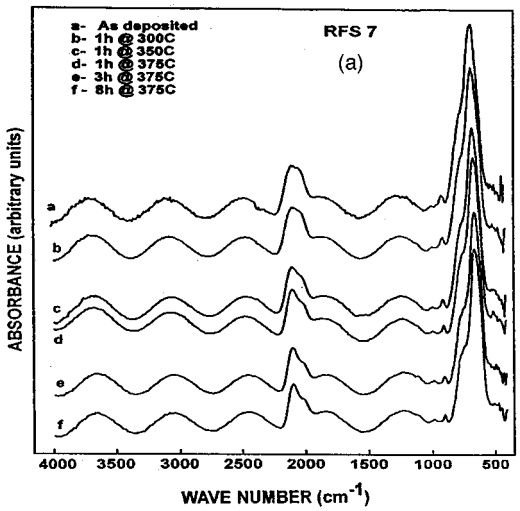

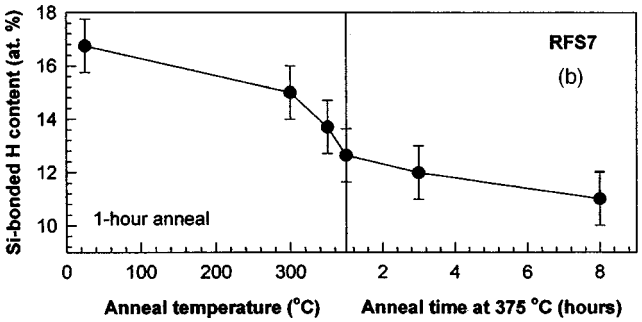

FIG. 14. (a) IR spectra of RFS7, as deposited and annealed sequentially for 1 hr at 300, 350, and 375 °C, followed by additional annealing for a total of 3 and 8 h at 375 °C. (b) Evolution of C_{Si-H} in RFS7, as determined by the evolution of the 640 cm^{-1} Si-H wagging mode band. Note that the behavior is similar to that of RFS3 and RFS4 which is shown in Figs. 11 and 12.

$\sim$770 cm^{-1} Si-CH_n and $\sim$1000 cm^{-1} C-H wagging strengthen relative to the $\sim$640 cm^{-1} Si-H wagging mode. Not surprising, this similar behavior suggests that the net transfer of H from Si- to C-bonded sites or its evolution as in RFS4, RFS, and RFS7, are common features of H dynamics in a-$Si_{1-x}C_x$:H (see Sec. IV below).

Figure 18 shows the deuterium level in the initially undeuterated layer, normalized to D_{max}, as a function of annealing time of ECR3 at 360 °C and ECR4 at 350 °C. Its growth in ECR3, where C_B $\sim$0.2 at. %, is faster than in ECR4, where C_B $\sim$0.6 at. %. This behavior is in stark contrast to the dramatic boron-induced enhancement of H diffusion in a-Si:H,[14] but consistent with the introduction of boron-induced nanovoids.[18]

TABLE VII. Fractional reduction in the Si-bonded H content C_{Si-H} ($\Delta C_{Si-H}/C_{Si-H}$) following annealing as shown in Figs. 11–14. Note the correlation with the initial nanovoid content C_{nV0} as determined from SAXS.

Sample	C_{nV0} (vol. %) ($\pm$0.1)	$\Delta C_{Si-H}/C_{Si-H}$ ($\pm$20%)	x (at. %) ($\pm$15%)
RFS3	0.5	20%	1.6
RFS5	0.7	32%	5.7
RFS7	0.9	34%	6.0
RFS4	0.9	50%	3.0

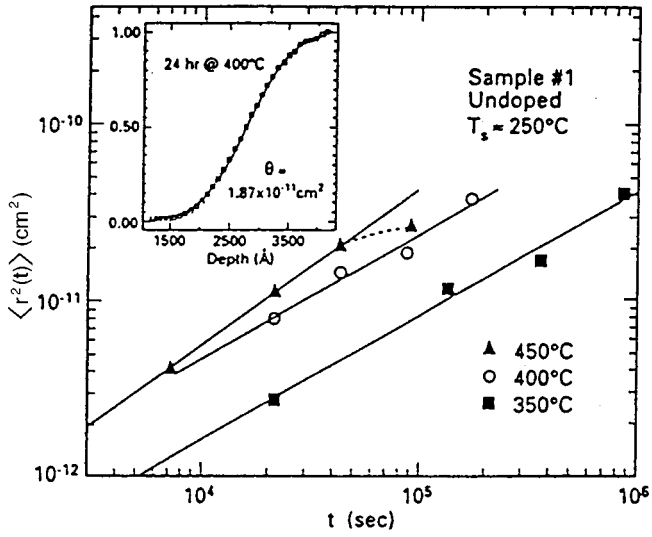

FIG. 15. $\log\langle r^2(t)\rangle$ vs log of annealing time t in undoped sample ECR1, annealed at 350, 400, and 450 °C.

Although not shown in Fig. 18, it should be noted that some diffusion into the undeuterated layer of the doped films occurred during growth: The as-deposited normalized D content $C_D/C_{D_{max}}$ of that layer in these films, about 0.01, was $\sim$10 times higher than $C_D/C_{D_{max}}$ in the undeuterated layer of the undoped films. In addition, the level in the latter did not change with annealing. This behavior is also discussed below.

IV. DISCUSSION

A. Microstructural dynamics of the RFS films

1. Microstructure of the as-Deposited RFS films

As described in Sec. III. A 1, the SAXS results clearly demonstrate that the as-deposited films have mass densities

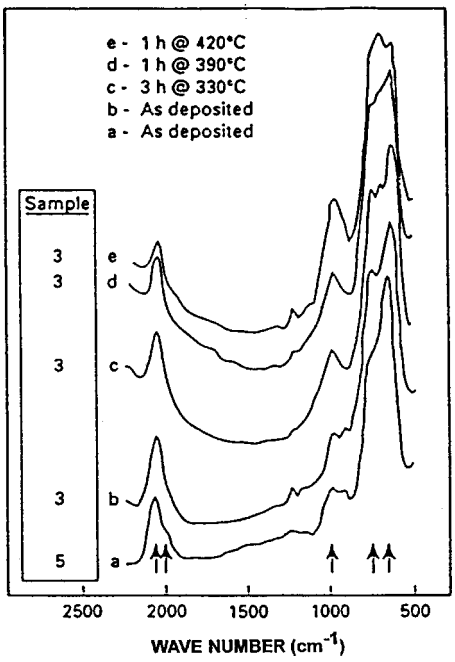

FIG. 16. IR spectra of as-deposited ECR5 and ECR3, and of ECR3 following the indicated annealing steps.

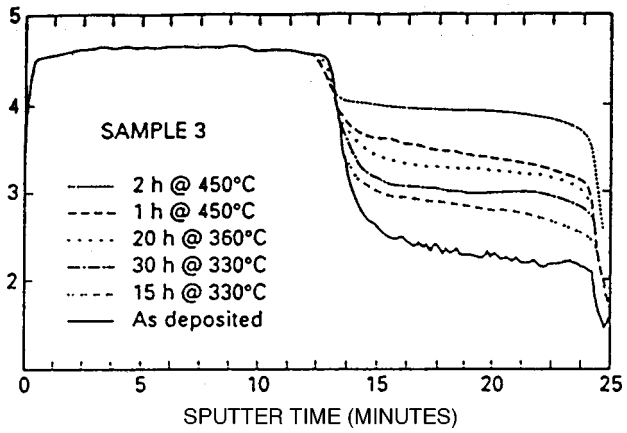

FIG. 17. SIMS depth profiles of sample ECR3, which contained $\sim$0.2 at. % boron (see Table II), annealed at $T \leqslant 450\,^{\circ}\mathrm{C}$ and normalized to the maximal D level.

that are 90–96% that of c-Si, residual columnarlike microstructures with columns $\geqslant$20 nm diameter, and 0.5–1.0 vol. % $\sim$1 nm-diameter nanovoids with no preferred shape or orientation, modeled as spheres. In comparison, *a*-Si:H films prepared under otherwise identical conditions had densities that were 96% that of c-Si, exhibited no columnar microstructure, and contained no more than 0.5 vol. % nanovoids when deposited at an rf power $P \geqslant 400$ W.[10] Hence it appears that in general, introduction of the carbon through the methane in the plasma promotes the formation of the columnar microstructure and the $\sim$1 nm diameter nanovoids. It is well known that the columnar microstructure is an inherent feature of the basic nucleation and growth process of *a*-Si:H films.[44] However, in GD films deposited at sufficiently high substrate temperatures ($\geqslant 250\,^{\circ}\mathrm{C}$) or RFS films deposited at sufficiently high-rf power ($\geqslant$300 W) this microstructure is eliminated by dynamical processes occurring during growth such as enhanced surface mobility or increased ion bombardment.[10,45,46] Hence it appears that the species derived from the methane in the plasma impede the process of elimination of the columnar microstructure. The strength of the C-H bond and consequent incorporation of CH_2 and CH_3 groups in the growing film, which probably promote the formation of nanovoids,[3,7,17,18,22,35] provide a plausible explanation for this scenario. However, other factors that affect the microstructural features are clearly present: sample RFS3 contained only 1.6 at. % carbon and its initial nanovoid content was only 0.5 vol. %, but its density was a relatively low 2.156 g/cm^3 or 92.5% of *c*-Si. On the other hand, sample RFS8 contained 7.1 at. % carbon and the same initial nanovoid content, and its density was a higher 2.233 g/cm^3 or 96% of *c*-Si. One possible factor competing with the CH_2- and CH_3-induced columnar microstructure and nanovoids may be the effect of tetrahedral (diamondlike) carbon bonding and CH groups in increasing the density of the network. Since we cannot determine the fraction of C atoms that are bonded to no more than one H atom, this suggestion remains speculative. However, it may be established or refuted by the fabrication and study of films with higher carbon content or thick films that yield a detectable C-H IR stretch vibration band circa 3000 cm^{-1}.

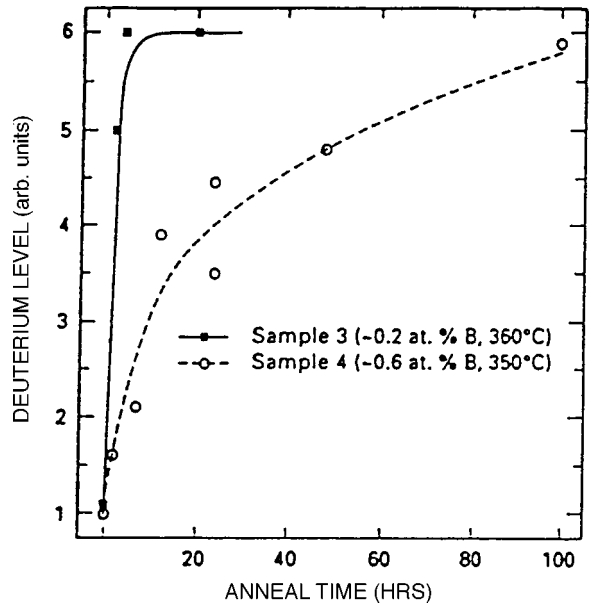

FIG. 18. The deuterium level in the initially undeuterated layers of ECR3 and ECR4, normalized relative to the level in the deuterated layer, as a function of annealing time of ECR3 at 360 °C and ECR4 at 350 °C.

Another interesting feature resulting from the analysis of the SAXS of the as-deposited RFS films is the suggested extent of the ''strain fields'' induced by the nanovoids, with an effective diameter of $\sim$1.7 nm in RFS4. Since the average diameter of the nanovoids themselves is 1.1 nm, the ''strain fields'' are very short-ranged. In addition, *a priori* we would expect the distorted tetrahedral network to be actually more relaxed around the nanovoids than deeper in the bulk of the network. The results of the SAXS analysis are also consistent with this picture in which the network is more relaxed around the nanovoids. Note that the range of the relaxation induced by the nanovoids is only of order $\sim$0.3 nm, or about one monolayer, which is consistent with the prevailing results of calculations of the network disorder about multivacancies and nanovoids.

2. Dynamics of the microstructure of the RFS films

As shown in Fig. 4 and Tables IV and V, and described in Sec. III A 2 above, the integrated SAXS of all the RFS films increased similarly with annealing. This increase of up to $\sim$100% was qualitatively similar to but considerably weaker than that of RFS *a*-Si:H, where it increased by $\sim$200% following similar annealing sequences.[10] Since these RFS *a*-Si:H samples included films with a more pronounced columnar microstructure than that of the films studied in this work, the weaker increase in C_{nV} cannot be attributed to this microstructure. Hence, it is suspected to be due to the strength of the Si-C and C-H bonds, which is greater than that of Si-Si and Si-H.

B. Hydrogen dynamics in the RFS films

1. Long-range atomic H motion and voids in the RFS films

The first obvious observation is the long-range motion of the D atoms and presumably of the H atoms as well, in sample RFS1, RFS2, and RFS3. The SAXS measurements

yielded nanovoid contents which increased with annealing from 1.0 to 1.6 vol. % in RFS2 and from 0.5 to 1.4 vol. % in RFS3. Previous work demonstrated that a sufficient nanovoid and microvoid content suppresses the long range atomic D and H motion, but the threshold value necessary to quench that motion was not determined.[17,20,22] However, it did appear that in quasicolumnar and columnar films the void content exceeded this threshold. This is plausible when considering the nature of this quenching phenomenon: the long-range atomic H motion observed by DSIMS is suppressed when the distance between any site on the Si network and the nearest surface is no more than the ~ 30 Å resolution of the SIMS, since H atoms on these surfaces typically recombine to molecular H_2 which does not redissociate. Yet the present results demonstrate that the H and D atoms still undergo long-range motion in films with a residual columnar microstructure and a nanovoid content which increases with annealing from 1.0 to 1.6 vol. % (in RFS2) and from 0.5 to 1.4 vol. % (in RFS3). Since α is much less than 1 in these films (see Sec. III A 3 and Table VI), it may be suspected that the boundaries of the residual columnarlike features are not as efficient in trapping and eliminating atomic H and D from the network as the surfaces of spherical-like nanovoids and microvoids. A possible scenario that would account for this observation is that of boundaries and nanovoid surfaces that are largely covered by saturated CH_n groups, which would inhibit trapping of diffusing atomic H or D.

2. Nature of the long-range atomic H motion in the RFS carbide films

The diffusion constant $D(t_L)$ for $L = 1000$ Å yields an activation energy of ~ 1.4 eV in RFS1, RFS2, and RFS3. This activation energy is similar to that of H diffusion in a-Si:H.[12,14–20,22] Hence, it appears that the incorporation of up to ~ 3 at. % carbon does not change E_a significantly. This conclusion can be readily understood within a scenario in which the carbon atoms are either bonded tightly to other Si and C atoms in the network, or are present as saturated CH_n groups at the boundaries of the residual columnar features or at the surfaces of nanovoids. Such carbon would probably interact less with the hopping H and D than Si with weak bonds to the network or with a dangling bond or an H atom at a nanovoid surface. As a consequence, H diffusion would be quantitatively similar to that found in a-Si:H.[12,14–17,19,20,22]

C. Hydrogen bonding and evolution from the RFS and ECR carbide films

As mentioned in Secs. III C and III E, the IR spectra of both RFS3 and the ECR films showed clearly that the C-bonded H content increases at the expense of the Si-bonded H. This net transfer results naturally from the strength of the C-H bond, which is greater than that of the Si-H bond. The IR spectra of all the RFS films also indicate hydrogen evolution. Figures 11–14 and 16 demonstrate that the H atoms whose stretch vibration mode is at 2000 cm^{-1}, i.e., embedded in the bulk of the Si network, contribute more to this process than those vibrating at 2080– 2150 cm^{-1}, i.e., those on void surfaces or bonded to Si-C or Si-O groups. This is also consistent with the greater trapping energy of the latter type of H atoms.

The results do not enable a quantitative comparison with the H-exchange model of Kemp and Branz.[30,31] However, they appear to be in qualitative agreement with it, since geometrical considerations would suggest that the probability of exchange of an H atom in a transport state with an atom on a surface is less than with a Si-bonded H atom embedded in the bulk of the network.

D. Hydrogen dynamics in undoped ECR a-$Si_{0.86}C_{0.14}$:H

The anomalously low-activation energy $E_a(1000\ \text{Å}) \sim 1.0$ eV of H and D in undoped ECR1 is not understood but clearly deserves attention since it is widely believed that the value of ~ 1.5 eV typically found in a-Si:H is related to the energy required to release an H atom from a Si-bonded site to the transport state. Hence, the present results could invoke a speculation that the H and D atoms diffusing through the undoped ECR films are trapped in shallower sites. While the evolution of the IR spectra of boron-doped ECR3 is similar to that of the RFS films, one cannot rule out the possibility that the IR of undoped ECR films may indicate a different behavior. This issue obviously warrants a more detailed SAXS, IR, and SIMS study of undoped ECR a-$Si_{1-x}C_x$:H.

E. Hydrogen dynamics in boron-doped ECR a-$Si_{086}C_{0.14}$:H

The DSIMS profiles of 0.2 at. % boron-doped ECR3 shown in Fig. 17 are sharp and ''unsmeared,'' but still consistent with complementary error-function profiles indicating that most of the D atoms do not undergo long-range motion. This is in contrast to the behavior of undoped ECR1, the undoped RFS carbides, and undoped and doped GD and RFS a-Si:H, and is very intriguing. On the one hand, boron doping is well-known to dramatically enhance the H diffusion constant in a-Si:H.[14,15,18] On the other hand, it is also well-known to induce hydrogen complexes in Si.[47] Therefore, the behavior shown in Fig. 17 may be due to slow release of the D atoms from deep traps in B-induced complexes in the initially deuterated top layer followed by fast diffusion among the transport states in the bottom layer. In other words, the relevant profile to be considered is the ''flat'' profile in the bottom layer, which is consistent with very fast diffusion. The DSIMS profiles shown in Fig. 18 may now be understood within this scenario: The boron level of 0.2 at. % in ECR3 is sufficient to enhance the diffusion in the bottom layer to a ''flat'' profile, but the increased boron content and B-induced H and D complexes in ECR4 cause a slower release of D atoms from the top layer. It is interesting to note that such complexes are apparently not sufficiently significant to yield such behavior in B-doped GD a-Si:H.[14,15] However, ECR a-Si:H does exhibit behavior indicative of enhanced B-induced deep H-trap formation, probably on B-induced nanovoids, and very fast diffusion among the transport states.[18] The recent results of Estes *et al.*,[48] which demonstrated a significant growth in nanovoid density with B doping of a-Si:H, are entirely consistent with this scenario. Finally, the behavior of the B-doped ECR carbides also appears to be in qualitative agreement with the hydrogen exchange model of Kemp and Branz,[30,31] but the results are not sufficiently detailed to enable a quantitative comparison with that model.

V. CONCLUSIONS

The results and their analysis described in this work lead to the following conclusions on RFS and ECR a-$Si_{1-x}C_x$:H:

(a) RFS carbide films, with as little as $x \sim 1.6$ at. % carbon, exhibit a residual columnar morphology, with columns $\geqslant 20$ nm in diameter, which are absent from a-Si:H deposited under similar conditions.[10] Since a columnar morphology is generally incipient in the nucleation and growth of a-Si:H thin films[44] but is destroyed by dynamical processes during growth under appropriate conditions, it appears that the carbon atoms strengthen it and render it more robust.

(b) The nanovoid volume of these films is 0.5–1.0 vol. %, which is considerably higher than in the comparable a-Si:H.[10]

(c) The columnar morphology and nanovoid volume lead to an overall film density of 2.12–2.23 gm/cm^3, i.e., 91–96% of the density of Si which is 2.33 g/cm^3. As the density of SiC is 3.22 g/cm^3, it appears that the primary structural effect of 1.6–19 at. % carbon is to induce a relatively robust columnar morphology and a relatively large concentration of nanovoids in the network, leading to a relatively low-density film.

(d) The evolution of the SAXS and the IR of the RFS carbide films following the annealing processes described above indicate that despite the net transfer of H atom from Si- to C-bonded sites, which is expected from the greater strength of the latter bond and hydrogen evolution, the network relaxation processes in these carbide films are significatly slower than those in the corresponding RFS a-Si:H and are largely manifest in a $\sim 20\%$ growth of the diameter of the average nanovoid. The slower network relaxation dynamics are entirely consistent with points (a)–(c) above.

(e) Earlier work on RFS a-Si:H demonstrated that a sufficient nanovoid and microvoid content suppresses long-ranged atomic H motion.[17,18,22] The results described in this work demonstrate that the nanovoid content of up to 1 vol. % and the residual columnar morphology of the carbide films are insufficient to suppress the long-range motion. As typical of a-Si:H, this motion was observed to be dispersive, i.e., the diffusion constant D depended on time as $D(t) = D_{00}(\omega t)^{-\alpha}$, where the dispersion parameter α varied from 0 to 0.5 ± 0.1 among the samples, but was temperature independent at $350\,^\circ \leqslant T \leqslant 475\,^\circ$C. This behavior contrasts that of a-Si:H, where α was shown to be strongly temperature dependent.[19,20,22,28] However, since it was also shown that α is strongly affected by network relaxation processes, its weak-temperature dependence in the carbide films is entirely consistent with the slower network dynamics as monitored by the SAXS measurements and mentioned above.

(f) The activation energies E_a for H diffusion length $L = 1000$ Å were similar to those measured previously for a-Si:H, but the diffusion in one of the RFS films exhibited an anomalously low $E_a(1000\ \text{Å}) \approx 0.65$ eV, which is not understood at present. These results suggest that H motion in these RFS carbide films is very similar to that in a-Si:H.

(g) As in the RFS3 film, annealing of the undoped ECR a-$Si_{0.86}C_{0.14}$:H films also induces a net transfer of H atoms from Si- to C-bonded sites, as expected from the greater strength of the latter bond. Evolution is observed from all the RFS films.

(h) H diffusion in the undoped ECR films also exhibited similar dispersive motion, but also with an anomalously low $E_a(1000\ \text{Å}) \approx 1.0$ eV, which is not understood at present. The dispersion parameter α descreased from ~ 0.3 at 350–400 °C to ~ 0.1 at 450 °C, whereas in a-Si:H it decreases up to $\sim 350\,^\circ$C but increases at higher temperatures.[20,28] This behavior is also consistent with slower network dynamics in the ECR films as compared to a-Si:H.

(i) Boron doping of the ECR carbide films was found to reduce the bulklike Si-bonded H content, suggesting that it induces nanovoids, which is consistent with its effects in Si (Ref. 47) and the observed trapping of most of the H and D atoms at deep sites. However, a small fraction of the H atoms apparently undergo very fast diffusion through transport states, reminiscent of B-doped a-Si:H.[14] The motion appears to be in qualitative agreement with the H exchange model of Kemp and Branz.[30,31]

VI. SUMMARY

Small angle x-ray scattering (SAXS), IR, and deuterium secondary-ion-mass spectrometry (DSIMS) studies of microstructure and H dynamics in rf-sputter-deposited (RFS) a-$Si_{1-x}C_x$:H ($1.6 \leqslant x \leqslant 19$ at. %) and electron-cyclotron resonance-deposited (ECR) a-$Si_{0.86}C_{0.14}$:H was described. The SAXS of the RFS films indicated a residual columnar morphology and a nanovoid content $0.5 \leqslant C_{nV} \leqslant 1.0$ vol. % in all of the RFS films. The larger-scale residual columnar microstructure was unaffected by annealing of up to 4 h at 420 °C but the integrated SAXS increased by $\sim 100\%$, indicating a similar increase in the nanovoid content. This increase was smaller than that exhibited by RFS a-Si:H, suggesting that the carbon atoms incorporated in the Si network weakened the network's relaxation processes. A detailed analysis of one of the typical SAXS intensity data sets indicated that this increase was due largely to a $\sim 20\%$ increase in the average diameter of a nanovoid from ~ 0.55 to ~ 0.65 nm. Assuming a strain field as the origin of the observed interference effect which results from correlated nanovoid positions, the SAXS-indicated range of the strain field was found to be only a few angströms or roughly one bond length.

In spite of the residual columnar morphology and a nanovoid content which reached ~ 1.6 vol. % in films with $x \leqslant 3$ at. %, their DSIMS depth profiles demonstrated long-range atomic H and D motion in agreement with a power-law time-dependent diffusion constant $D(t) = D_{00}(\omega t)^{-\alpha}$, with low or moderate values of the dispersion parameter α. The dependence of α on the annealing temperature was weaker than that observed in a-Si:H, also consistent with weaker network relaxation dynamics. The activation energy for diffusion over a diffusion length of 1000 Å $E_a(1000\ \text{Å})$ was ~ 1.7 and ~ 1.4 eV in two films, which is similar to the values found in a-Si:H, but an anomalously low ~ 0.65 eV in a third sample. The IR measurements indicated that the Si-bonded H content C_{Si-H} deceased by 20% - 50% over these annealing periods. The fractional reduction in C_{Si-H} appeared to be correlated with C_{nV}, as expected since the distance from any given Si-H bond to the nearest surface decreases with increasing C_{nV}.

The IR measurements on some RFS and ECR films

also demonstrated that during annealing C_{Si-H} decreases relative to the C-bonded H content C_{C-H}, which is also expected from the greater strength of the C-H bond relative to the Si-H bond. Hydrogen evolution from the RFS films is also observed. In addition, the reduction in the $\sim 2000\ \mathrm{cm}^{-1}$ Si-H stretch vibration band, characteristic of H embedded in the network, was greater than that of the 2080–2150 cm^{-1} bands, characteristic of surface Si-H, C-Si-H, and O-Si-H groups. This behavior is also consistent with the migration of Si-bonded H from the bulk to deeper sites at the void surfaces. It is also in qualitative agreement with the hydrogen exchange model of Kemp and Branz.[30,31]

While the DSIMS of the annealed undoped ECR films exhibited the normal complementary error function profiles with low values of α and were also consistent with network dynamics, which are weaker than those of a-Si:H, they also yielded an anomalously low $E_a(1000\ \text{Å}) \sim 1.0$ eV, which is not understood at present. The DSIMS profiles of the boron-doped ECR films indicated that most of the H and D atoms were deeply trapped, possibly at surfaces of B-induced voids and B-induced complexes, but they are also consistent with fast diffusion of a small fraction of the H and D atoms among transport states, reminiscent of the B-induced enhanced H diffusion in a-Si:H. The evolution of the DSIMS of the B-doped ECR films also appeared to be in qualitative agreement with the H-exchange model of Kemp and Branz.[30,31]

ACKNOWLEDGMENTS

J.S. and R.S. thank Dr. H. Branz for valuable discussions. D.L.W. gratefully acknowledges the support of NREL through subcontract No. RAN-4-13318-04. H.K. thanks the Scientific and Technical Research Council of Turkey for partial support. Ames Laboratory is operated by Iowa State University for the U.S. Department of Energy under Contract No. W-7405-Eng-82. This work was supported by the Director for Energy Research, Office of Basic Energy Sciences.

[1] R. Vanderhaghen, B. Chaurand, and B. Drevillon, Thin Solid Films **124**, 293 (1985).
[2] A. J. Craven, A. M. Patterson, A. R. Long, and J. I. B. Wilson, J. Non-Cryst. Solids **77&78**, 217 (1985).
[3] A. H. Mahan, D. L. Williamson, B. P. Nelson, and R. S. Crandall, Sol. Cells **27**, 465 (1989).
[4] A. H. Mahan, Y. Chen, D. L. Williamson, and G. D. Mooney, J. Non-Cryst. Solids **137&138**, 65 (1991).
[5] S. Muramatsu, T. Shimada, H. Kajiyama, K. Azuma, T. Watanabe, T. Kamiyama, and K. Suzuki, Jpn. J. Appl. Phys., Part 2 **28**, L1092 (1989).
[6] S. J. Jones, Y. Chen, D. L. Williamson, R. Zedlitz, and G. Bauer, Appl. Phys. Lett. **62**, 3267 (1993).
[7] D. L. Williamson, A. H. Mahan, B. P. Nelson, and R. S. Crandall, Appl. Phys. Lett. **55**, 783 (1989).
[8] M. N. P. Carreno, I. Pereyra, M. C. A. Fantini, H. Takahashi, and R. Landers, J. Appl. Phys. **75**, 538 (1994).
[9] D. L. Williamson, in *Amorphous Silicon Technology—1995*, edited by M. Hack, E. A. Schiff, A. Madan, M. Powell, and A. Matsuda, MRS Symposia Proceedings No. 377 (Materials Research Society, Pittsburgh, PA, 1995), p. 251.
[10] J. Shinar, H. Jia, R. Shinar, Y. Chen, and D. L. Williamson, Phys. Rev. B **50**, 7358 (1994).
[11] S. Acco, D. L. Williamson, P. A. Stolk, F. W. Saris, M. J. van den Boogaard, W. C. Sinke, W. F. wan der Weg, S. Roorda, and P. C. Zalm, Phys. Rev. B **53**, 4415 (1996).
[12] D. E. Carlson and C. W. Magee, Appl. Phys. Lett. **33**, 81 (1978).
[13] W. Beyer, in *Tetrahedrally-Bonded Amorphous Semiconductors*, edited by D. Adler and H. Fritsche (Plenum Press, New York 1985), p. 129.
[14] R. A. Street, C. C. Tsai, J. Kakalios, and W. B. Jackson, Philos. Mag. B **56**, 305 (1987).
[15] J. Kakalios, R. A. Street, and W. B. Jackson, Phys. Rev. Lett. **59**, 1037 (1987).
[16] W. B. Jackson, Phys. Rev. B **38**, 3595 (1988).
[17] J. Shinar, R. Shinar, S. Mitra, and J.-Y. Kim, Phys. Rev. Lett. **62**, 2001 (1989).
[18] S. Mitra, R. Shinar, and J. Shinar, Phys. Rev. B **42**, 6746 (1990).
[19] X.-M. Tang, J. Weber, Y. Baer, and F. Finger, Phys. Rev. B **41**, 7945 (1990).
[20] X.-M. Tang, J. Weber, Y. Baer, and F. Finger, Phys. Rev. B **42**, 7277 (1990).
[21] P. V. Santos, N. M. Johnson, and R. A. Street, Phys. Rev. Lett. **67**, 2686 (1991).
[22] J. Shinar, R. Shinar, X.-L. Wu, S. Mitra, and R. F. Girvan, Phys. Rev. B **43**, 1631 (1991).
[23] W. Beyer, Physica B **170**, 105 (1991).
[24] W. Beyer, J. Herion, H. Wagner, and U. Zastrow, in *Amorphous Silicon Technology—1991*, edited by A. Madan, Y. Hamakawa, M. J. Thompson, P. C. Taylor, and P. G. LeComber, MRS Symposia Proceeding No. 219 (Materials Research Society, Pittsburgh, PA, 1991), p. 75.
[25] W. B. Jackson and C. C. Tsai, Phys. Rev. B **45**, 6564 (1992).
[26] H. M. Branz, S. E. Asher, and B. P. Nelson, Phys. Rev. B **47**, 7061 (1993).
[27] P. V. Santos, N. M. Johnson, R. A. Street, M. Hack, R. Thompson, and C. C. Tsai, Phys. Rev. B **47**, 10 244 (1993).
[28] R. Shinar, J. Shinar, H. Jia, and X.-L. Wu, Phys. Rev. B **47**, 9361 (1993).
[29] P. Hari, P. C. Taylor, and R. A. Street, in *Amorphous Silicon Technology—1995*, (Ref. 9), p. 479.
[30] M. Kemp and H. M. Branz, Phys. Rev. B **47**, 7067 (1993).
[31] M. Kemp and H. M. Branz, Phys. Rev. B **52**, 13 946 (1995).
[32] J. Crank, *The Mathematics of Diffusion* (Clarendon Press, Oxford, 1975), Chap. 2.
[33] V. Halpern, Phys. Rev. Lett. **67**, 611 (1991).
[34] S. Roorda, S. Doorn, W. C. Sinke, P. M. L. O. Scholte, and E. van Loenen, Phys. Rev. Lett. **62**, 1880 (1989).
[35] M. L. Albers, J. Shinar, and H. R. Shanks, J. Appl. Phys. **64**, 1859 (1988).
[36] R. Shinar, J. Shinar, G. Subramania, H. Jia, S. Sankaranarayanan, M. Leonard, and V. L. Dalal, in *Amorphous Silicon Technology –1994*, edited by E. A. Schiff, M. Hack, A. Madan, M. J. Powell, and A. Matsuda, MRS Symposia, Proceeding No. 336 (Materials Research Society, Pittsburgh, PA, 1994), pp. 317–322.
[37] R. D. Knox, V. L. Dalal, B. Moradi, and G. Chumanov, J. Vac.

Sci. Technol. A **11**, 1896 (1993).
[38] M. Cardona, Phys. Status Solidi B **118**, 463 (1983).
[39] D. R. McKenzie, J. Phys. D **18**, 1935 (1985).
[40] A. Sproul, D. R. McKenzie, D. J. H. Cockayne, Philos. Mag. B **54**, 113 (1986).
[41] K. Eberhardt, E. Lotter, M. Heintze, H.-D. Mohring, and G. H. Bauer, in *Amorphous Si Technology—1992*, edited by A. Madan, M. J. Thompson, Y. Hamakawa, E. A. Schiff, and P. G. LeComber, MRS Symposia Proceedings No. 258 (Materials Research Society, Pittsburgh, PA, 1992), p. 269.
[42] L. A. Fegin and D. I. Svergun, *Structure Analysis by Small-Angle X-Ray and Neutron Scattering* (Plenum Press, New York, 1987).
[43] R. Triolo, E. Caponetti, and S. Spooner, Phys. Rev. B **39**, 4588 (1989).
[44] R. W. Collins and J. M. Cavese, J. Appl. Phys. **61**, 1869 (1987); **61**, 1662 (1987); in *Amorphous Silicon Technology*, edited by A. Madan, M. J. Thompson, P. C. Taylor, P. G. LeComber, and Y. Hamakawa, MRS Symposia Proceeding No. 118 (Materials Research Society, Pittsburgh, PA, 1988), p. 19.
[45] A. R. Middya, S. Ray, S. J. Jones, and D. L. Williamson, J. Appl. Phys. **78**, 4966 (1995).
[46] P. Wickboldt, D. Pang, W. Paul, J. H. Chen, F. Zhong, C.-C. Chen, J. D. Cohen, and D. L. Williamson, J. Appl. Phys. **81**, 6252 (1997).
[47] *Hydrogen in Semiconductors*, Vol. 34, edited by J. I. Pankove and N. M. Johnson, Semiconductors and Semimetals (Academic Press, New York, 1991); A. A. Bonapasta, P. Giannozzi, and M. Capizzi, Phys. Rev. B **45**, 11 744 (1992).
[48] M. J. Estes, L. R. Hirsch, S. Wichart, G. Moddel, and D. L. Williamson, J. Appl. Phys. **82**, 1832 (1997).